ceramics

MDPI

Article

Compressive Creep Measurements of Fired Magnesia Bricks at Elevated Temperatures Including Creep Law Parameter Identification and Evaluation by Finite Element Analysis

Guenter Unterreiter [1,*], Daniel R. Kreuzer [2], Bernd Lorenzoni [1], Hans U. Marschall [1], Christoph Wagner [2], Robert Machhammer [1] and Gernot Hackl [1]

[1] RHI Magnesita, Technology Center Leoben, 8700 Leoben, Austria; Bernd.Lorenzoni@RHIMagnesita.com (B.L.); Ulrich.Marschall@RHIMagnesita.com (H.U.M.); Robert.Machhammer@RHIMagnesita.com (R.M.); Gernot.Hackl@RHIMagnesita.com (G.H.)

[2] RHI Magnesita, Technology and Support, 1120 Vienna, Austria; Daniel.Kreuzer@RHIMagnesita.com (D.R.K.); Christoph.Wagner@RHIMagnesita.com (C.W.)

* Correspondence: Guenter.Unterreiter@RHIMagnesita.com; Tel.: +43-502-13-5180

Received: 19 December 2019; Accepted: 14 April 2020; Published: 22 April 2020

Abstract: Creep behavior is very important for the selection of refractory materials. This paper presents a methodology to measure the compressive creep behavior of fired magnesia materials at elevated temperatures. The measurements were carried out at 1150–1500 °C and under compression loads from 1–8 MPa. Creep strain was calculated from the measured total strain data. The obtained creep deformations of the experimental investigations were subjected to detailed analysis to identify the Norton-Bailey creep law parameters. The modulus of elasticity was determined in advance to simplify the inverse estimation process for finding the Norton-Bailey creep parameters. In the next step; an extended material model including creep was used in a finite element analysis (FEA) and the creep testing procedure was reproduced numerically. Within the investigated temperature and load range; the creep deformations calculated by FEA demonstrated a good agreement with the results of the experimental investigations. Finally; a finite element unit cell model of a quarter brick representing a section of the lining of a ferrochrome (FeCr) electric arc furnace (direct current) was used to assess the thermo-mechanical stresses and strains including creep during a heat-up procedure. The implementation of the creep behavior into the design process led to an improved prediction of strains and stresses.

Keywords: compressive creep; Norton-Bailey; creep law parameter identification; finite element analysis; fired magnesia bricks

1. Introduction

Material selection is a crucial stage in the engineering of structural components in complex furnaces and refractory linings (Figure 1). Optimized operating conditions, greater output and efficiencies push refractories to their physical limits. Therefore, high-performing refractory products combined with sophisticated material models are needed to predict the in-service performance. Although significant information is available on the effect of additives, corrosion process and thermal behavior of refractories [1,2], significantly less data exists on the creep response of refractories at elevated temperatures in the range of 1200–1500 °C.

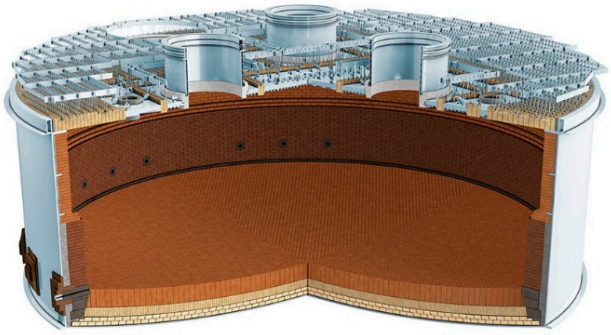

Figure 1. Refractory lining of an electric arc furnace for the non-ferrous and ferroalloy industry.

In material science, creep is defined as the deformation of a material over a period of time due to the combined influence of temperature and an applied load [3]. If a specimen is loaded with a pressure at high temperature, a time-dependent strain is observed as illustrated in Figure 2. After a spontaneous elastic strain (ϵ_0), three creep stages are differentiated, the so-called primary (I), secondary (II) and tertiary (III) creep stages (Figure 2) [4].

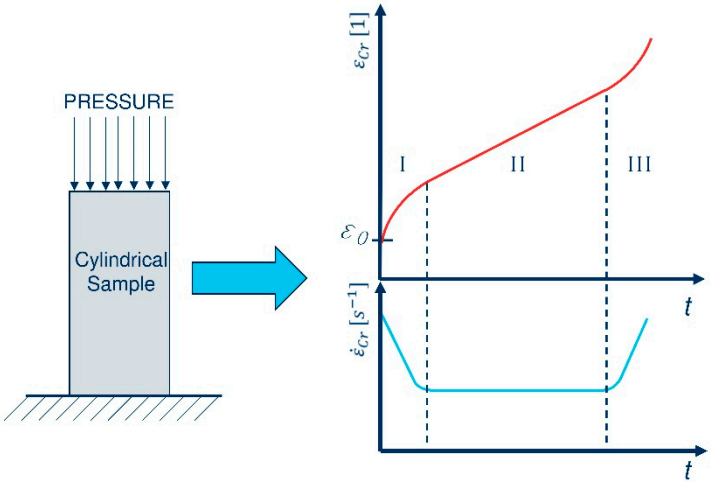

Figure 2. Typical shape of a three-region creep curve showing creep strain (ε_{Cr}) and strain rate ($\dot{\varepsilon}_{Cr}$).

However, it should be noted that most refractory structures are not subjected to creep under constant load. In most cases, the global loads, not considering local stresses, e.g., due to thermal shock, are caused by restrictions of the refractories' thermal expansions due to the rigid external structures (e.g., steel shell). In this case, the creep of the material will result in a decrease in the load. Once the suppressed thermal expansion is compensated by creep, there is no significant load on the material and the creep process is stopped before reaching tertiary creep stage, which would result in the failure of the structure. In some unique cases, e.g., in a regenerator superstructure, the weight load of the checker bricks in combination with elevated temperatures could cause stresses relevant for creep that will not disappear with increasing deformation. Hence, special care has to be taken when selecting materials for such structures in order to avoid creep-induced failure. A different creep behavior between compression and tensile load is called asymmetric creep. The strain rate is therefore higher in tension than in compression [5]. Asymmetric creep has been documented for many materials, including ceramics [6,7]. The creep behavior for geomaterials (e.g., concrete, soil and rock) depends also on the average pressure load; in order to describe this material behavior, several viscoplastic models have been developed [8]. None of these models is able to describe the significant differences in creep behavior observed between tension and compression for multiphase ceramics

such as refractories [5]. Sophisticated methods have been proposed to characterize the asymmetrical creep behavior, as can be seen in the literature [9,10]. In this study, the creep calculation of the lining addressed the heat-up process, where compressive creep is mainly expected, and therefore asymmetric creep was not considered. The creep testing device (CTD) for high-temperature uniaxial compressive creep application and an efficient methodology to identify the creep law parameters used in this work were developed by the Chair of Ceramics (Montanuniversität, Leoben, Austria) [11].

Finite element modelling is increasingly used as an integral part of creep analysis for the integrity assessment of high-temperature structures. There are a variety of creep models which can be selected for implementation in finite element codes [12]. In this study, a Norton-Bailey creep model in the strain hardening formulation was used for the following reasons. The Norton-Bailey creep law can be used to describe the behavior in all three creep stages, it is a differential approach which includes the stress dependency on the creep behavior and it can be implemented in finite element programs for the simulation of transient stress states in refractories [13]. The applicability of the Norton-Bailey creep equation to characterize the creep behavior of refractories has been proven by previous studies [10,11,14].

2. Materials and Methods

In order to understand and predict the material behavior and the performance of refractory superstructures in operating furnaces, accurate engineering creep data are needed. Refractory creep can be adequately described by the Norton-Bailey creep law (Equation (1)). According to the Norton-Bailey strain hardening/softening formulation, the creep strain rate is a function of temperature, stress and creep strain:

$$\dot{\varepsilon} = K(T) \cdot \sigma^n \cdot \varepsilon_{cr}^a \tag{1}$$

Exponent a in the case of strain hardening (primary creep) is negative and for strain softening (tertiary creep) it is positive. Secondary creep occurs if the strain exponent a is equal to zero. The parameter K is a temperature function and n is the stress exponent [11]. The tertiary creep contribution is of minor importance for the design, as tertiary creep is followed by failure of the component and should be avoided [4]. In this research, the contribution of the secondary and tertiary creep stages was neglected, and the creep strain was described by primary creep.

The measurement results in this work include the elastic and viscoplastic creep deformation. Hence, the creep strain ε_{cr} must be derived from the uniaxial mechanical strain ε_{mech} (Equation (2)).

$$\varepsilon_{cr} = \varepsilon_{mech} - \frac{\sigma}{E} \tag{2}$$

The total strain ε_{tot} is composed of the thermal strain ε_{th}, the elastic strain ε_{el} and the creep strain ε_{cr}. In the case of compression, the mechanical strain and stress are negative. Hence under compression the absolute value of the creep strain ε_{cr} reduces the absolute value of the total strain (3).

$$\varepsilon_{tot} = \varepsilon_{th} + \varepsilon_{el} + \varepsilon_{cr} \tag{3}$$

The applied stress is σ and E is the Young's modulus. The exact procedure to identify the parameters K, n and a for the Norton-Bailey creep law has been described in [11]. The chemical composition of the fired magnesia brick under research is shown in Table 1.

Table 1. Average chemical composition in weight percent of the magnesia brick under research.

Brand	MgO	Al_2O_3	Fe_2O_3	CaO	SiO_2
A	97.2	0.1	0.2	1.9	0.6

As previously mentioned, the high-temperature compressive creep testing device was developed by the Chair of Ceramics at Montanuniversität Leoben, Austria. One creep testing device is located at the Technology Center Leoben. The main component is an electrical furnace that is equipped with molybdenum disilicide heating elements, push rods and corundum extensometers. An internal view of the furnace is shown in Figure 3.

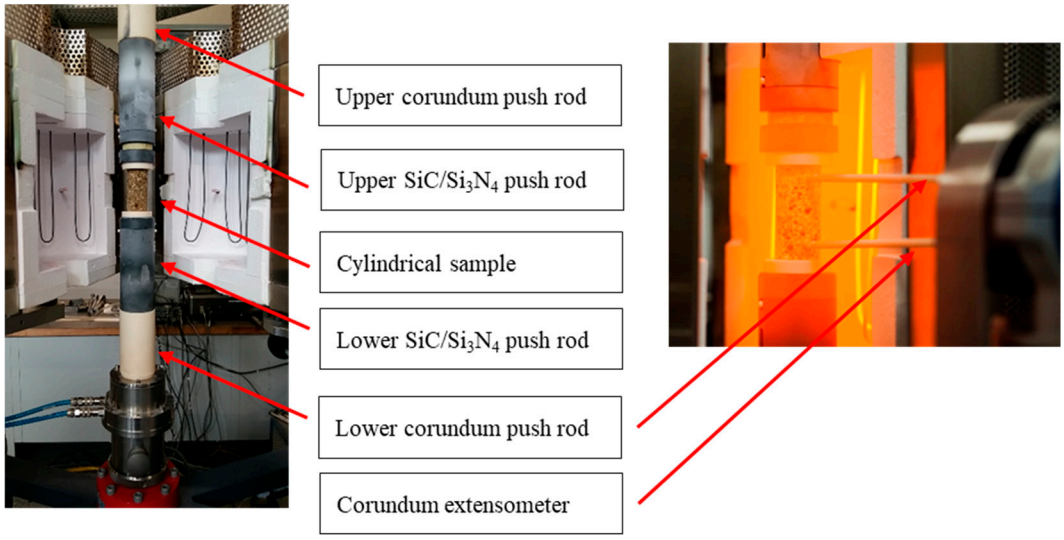

Figure 3. Internal view of the high-temperature compressive creep testing device located in the Research and Development Center Leoben.

Two platinum-rhodium thermocouples were used to measure the temperature. The first was located near the specimen to monitor the temperature and the second was installed close to the heating elements to control the furnace temperature. The loading was achieved with a spindle and measured by a load cell. The deformation was measured by two pairs of corundum extensometers with an initial leg distance of 50 mm; these pairs were placed in front and at the rear of the sample. The total strain data measured by each of these two extensometer pairs were recorded and the average values were used for further calculations. For the creep tests, cylindrical samples with a diameter of 35 mm and a height of 70 mm were used and a preload of 100 N (0.104 MPa) was applied axially to fix the sample (Figure 4).

Figure 4. Cylindrical specimen for compressive creep test.

The height/diameter ratio of two was suitable for deformation measurement in a zone of the specimen that was not affected by friction from the cylinder's front surfaces [11]. The furnace was heated at 10 K/min to a defined temperature followed by a dwell time of 30 min to reach isothermal

conditions in the cylinder. Afterwards, the two extensometer pairs were attached to the specimen's surfaces, then a defined load was applied by lifting the lower crosshead. During measuring, this load was maintained as a constant for the whole testing period of 5 h. The measurements were carried out in between the temperature range of 1150 °C up to 1500 °C, this range represents the conditions of use. The two extensometer pairs recorded the deformation due to compression. Therefore, based on these data a total strain-time curve under constant load and temperature was obtained. For a specific temperature, different compression loads were used, resulting in characteristic total strain/time curves as shown in Figure 5.

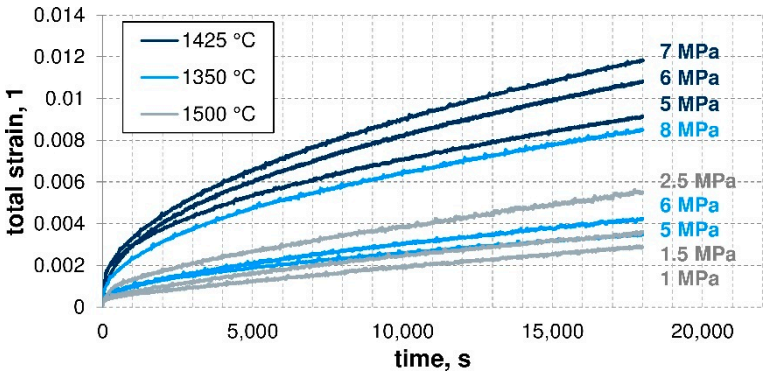

Figure 5. Total strain–time curves of the fired magnesia brick from experiments at 1350 °C, 1425 °C and 1500 °C and with varying compressive loads between 1 and 8 MPa.

These curves were used to evaluate the Norton-Bailey creep law parameters by inverse estimation. The transient testing procedure was simulated with finite element analysis using the Abaqus CAE 2018.HF4 software package (Dassault Systèmes, Vélizy-Villacoublay, France). Therefore, the determined creep law parameters were used in the von Mises stress-based Norton-Bailey creep model. For this purpose, a simplified two-dimensional axisymmetric model was used for modelling the radial symmetry of the specimen geometry (Figure 6).

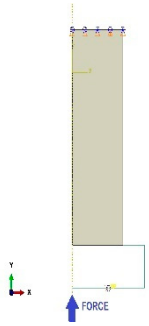

Figure 6. Schematic overview of the 2D axisymmetric finite element model for the virtual creep test procedure.

The mesh consisted of 564 coupled temperature-displacement elements. The top of the geometry was constrained in the y-direction and against rotation around the z-axis. For the simulation, a time-dependent uniaxial load (force) was introduced via a rigid body; the magnitude of the modelled force was detected by a load cell during the compression creep test. The total strain curves gained from the simulation were compared with the experimental results (Figure 5). In the next step, a three-dimensional thermo-mechanical finite element analysis of a quarter brick during heat up was conducted (see Figure 7). As previously mentioned, during the heat-up process, compressive creep was mainly expected, hence the uniaxial creep parameters were used for the multiaxial model. In the

numerical model, a quarter brick was representing a section of the lining of an electric arc furnace (shown in Figure 1). As shown in Figure 7a, the model consists of a quarter-brick section, a volume fraction of the ramming mix and a fraction of the steel shell. The internal radius from the center of the furnace to the hot side of the brick was 7.5 m. As seen in Figure 7b, the geometry was meshed with 27,144 hexahedral, 8-node thermally coupled elements (C3D8T), and the Abaqus CAE 2018.HF4 software package was used for running a fully coupled thermal stress analysis.

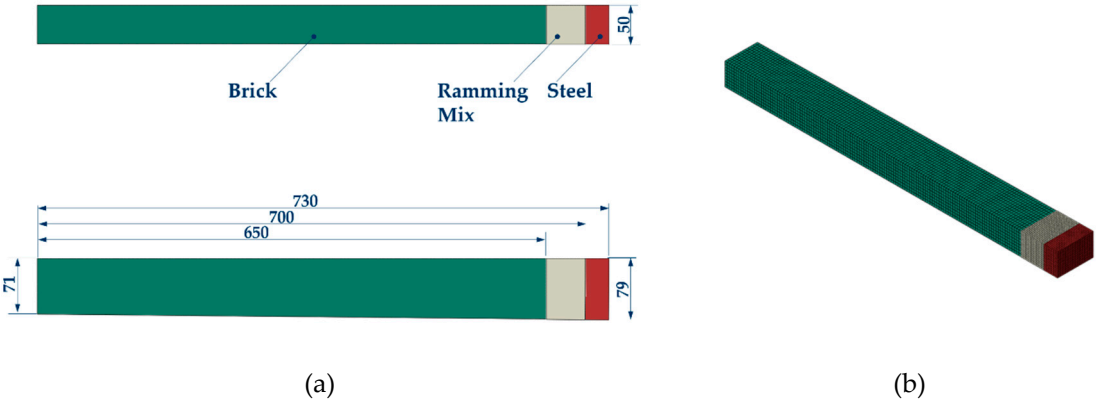

Figure 7. (**a**) Overview and dimensions in mm of the quarter brick, volume fraction of the ramming mix and steel shell. (**b**) Perspective view of the meshed quarter-brick model.

In order to quantify the influence of creep, an additional linear elastic model was used. This approach satisfied the needs for a qualitative comparison of the stresses in the steel shell based on the two previously specified material models. The thermal boundary conditions are shown in Figure 8.

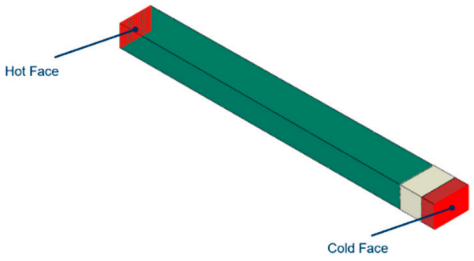

Figure 8. Thermal boundary conditions of the finite element quarter-brick model.

On the hot face, a mixed boundary condition with a heat transfer coefficient of 800 $W \cdot m^{-2} \cdot K^{-1}$ was used. Therefore, a time-dependent ambient temperature $T_{a,\,hot}(t)$, convective heat transfer and radiation were assumed. On the cold face, constant ambient temperature $T_{a,\,cold}$ with 50 °C and a heat transfer coefficient of 5000 $W \cdot m^{-2} \cdot K^{-1}$, representing water cooling, were modelled. The heat transfer coefficient between the brick and the ramming mix and between the ramming mix and the steel was 1000 $W \cdot m^{-2} \cdot K^{-1}$. The transient heat flow through the hot and cold faces by convection is shown in Equation (4):

$$\dot{Q}_c(t) = A \cdot h_c(T_a(t) - T_w(t)) \quad (4)$$

The heat transfer area A is in m^2, T_w is the surface temperature of the hot or cold face in °C. The heat transfer coefficient is h_c in $W \cdot m^{-2} \cdot K^{-1}$. The transient radiative heat transfer used only for the hot face

is given by Equation (5), where ε is the emissivity and σ is the Stefan-Boltzmann constant with the value of 5.67×10^{-8} (W·m^{-2}·K^{-4}):

$$\dot{Q}_r(t) = A \cdot \varepsilon \cdot \sigma \left(T_w^4(t) - T_a^4(t) \right) \tag{5}$$

In the cartesian coordinate system, the transient temperature field of the structure is described by Equation (6), where ρ is the material density (kg·m^{-3}), c is the specific heat of the materials (J·kg^{-1}·K^{-1}) and λ represents the materials' thermal conductivity in W·m^{-1}·K^{-1}. The temperature T is in ° C and x, y and z are the three spatial directions in m:

$$\rho c \frac{\partial T}{\partial t} = \frac{\partial}{\partial x}\left(\lambda \frac{\partial T}{\partial x}\right) + \frac{\partial}{\partial y}\left(\lambda \frac{\partial T}{\partial y}\right) + \frac{\partial}{\partial z}\left(\lambda \frac{\partial T}{\partial z}\right) \tag{6}$$

In Figure 9a, the symmetry boundary conditions are shown. To consider the compressibility of the joints between bricks in the real lining, a gap of 0.5 mm between brick and rigid wall was modelled (shown in Figure 9b). During the heat up, this joint closes, due to thermal expansion, which creates large stresses in the brick. For the other faces normal to the circumferential direction, a rotational symmetry boundary condition was used, and the bottom faces of the brick, ramming mix and steel shell were constrained in the vertical direction. The whole structure was not constrained at all in the radial direction.

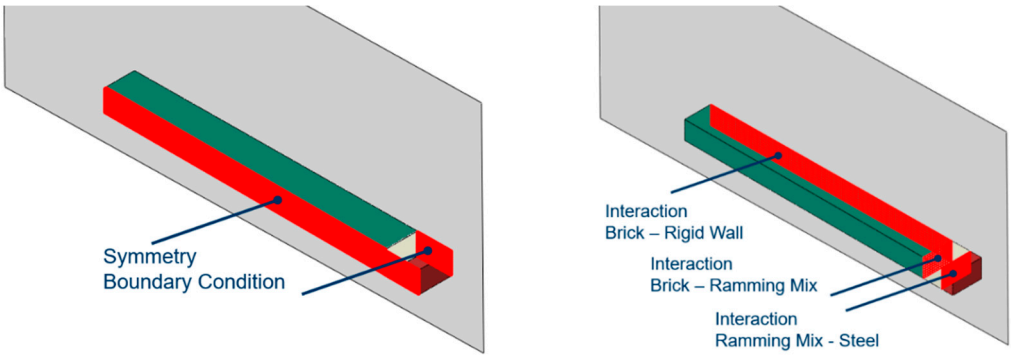

(a) (b)

Figure 9. Mechanical boundary conditions of the finite element model quarter-brick model: (**a**) symmetry boundary condition; (**b**) interaction between individual parts and rigid surface.

In Tables 2–4, the temperature-dependent physical properties of the considered materials are provided.

Table 2. Temperature-dependent specific heat of materials in J·kg^{-1}·K^{-1}.

Material	20 °C	100 °C	200 °C	500 °C	1500 °C	1800 °C
Brick	750	890	970	1110	1260	1200
Ramming Mix	710	930	1170	1630	2020	2050
Steel	430	500	540	690		

Table 3. Temperature-dependent thermal conductivity of materials in $W \cdot m^{-1} \cdot K^{-1}$.

Material	20 °C	100 °C	200 °C	500 °C	750 °C	1000 °C
Brick				4.55	3.95	3.65
Ramming Mix	16					16
Steel	57	57	54	42		

Table 4. Physical data of materials used in the model.

Material	Density ($kg \cdot m^{-3}$)	Young's Modulus (GPa)	Poisson's Ratio (1)	Thermal Expansion Coefficient ($10^{-6} \cdot K^{-1}$)
Brick	3400	17	0.2	7.9
Ramming Mix	1730	10	0.2	3
Steel	7850	209	0.28	12

In the case where no data were available for a specific temperature, the given values were extrapolated to higher or lower temperatures.

3. Results

The creep curves shown in Figure 5 were utilized for the determination of the creep parameters. Therefore, a damped least square method (Levenberg–Marquardt [15]) was carried out. The aim of the aforementioned least square method was to inversely estimate the corresponding Norton-Bailey creep law parameters K, n and a that are listed in Table 5.

Table 5. Norton-Bailey creep law parameters of the fired magnesia brick at different temperatures.

T (°C)	K ($MPa^{-n}s^{-1}$)	n	a
1350	9.11×10^{-14}	4.60	−1.07
1425	5.52×10^{-11}	1.55	−1.24
1500	8.98×10^{-10}	1.39	−0.75

The experimental and simulated total strain curves for a specific temperature and three different compression loads versus overall testing time are shown in Figures 10–12.

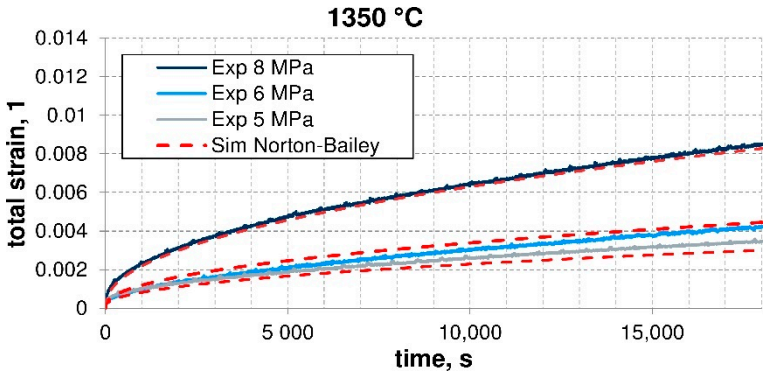

Figure 10. Total strain–time curves of the fired magnesia brick from experiment and numerical simulation using the Norton-Bailey creep law at 1350 °C and 5, 6 and 8 MPa compressive loads.

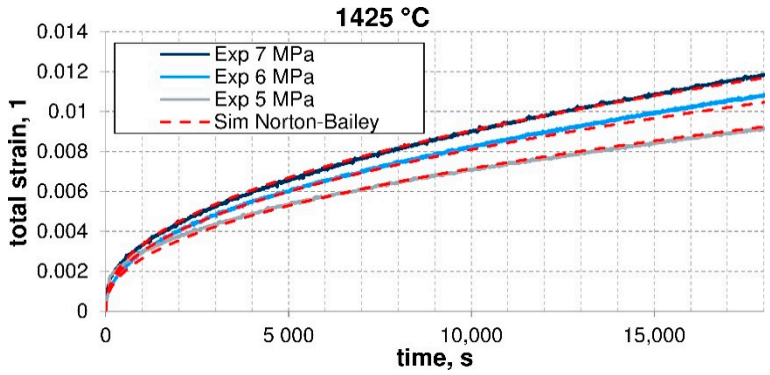

Figure 11. Total strain–time curves of the fired magnesia brick from experiment and numerical simulation using the Norton-Bailey creep law at 1425 °C and 5, 6 and 7 MPa compressive loads.

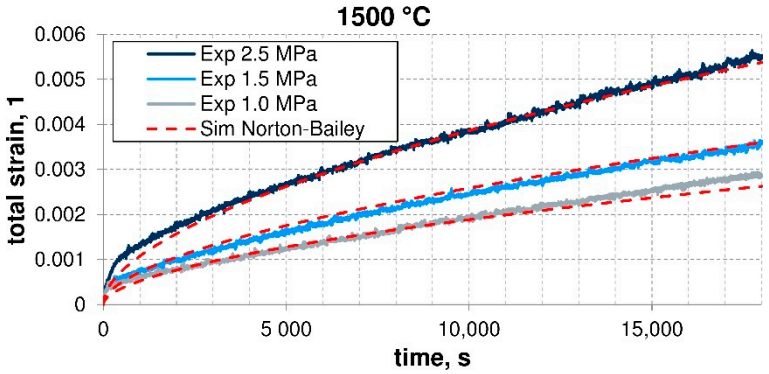

Figure 12. Total strain–time curves of the fired magnesia brick from experiment and numerical simulation using the Norton-Bailey creep law at 1500 °C and 1.0, 1.5 and 2.5 MPa compressive loads.

The measured strain curves in Figure 11 for the temperature 1425 °C at 15,000 s with a load of 5 MPa provoke a nearly three times higher total strain than at 1350 °C. A significant differentiation of the total strain/time curves even with 1 MPa compression load difference can be observed at 1425 °C.

Further increasing the testing temperature to 1500 °C which is shown in Figure 12 resulted in a good differentiation of the strain/time curves at load differences of 0.5 MPa. The simulated curves show for all three testing temperatures a satisfactory agreement with the measurement. As seen in Table 5, the value of K at 1350 °C is three powers of ten larger than that for 1425 °C, whereas between 1425 °C and 1500 °C the distinction of K is only one power of ten.

As shown in Figure 13, the curves generated for 5 and 6 MPa have a similar progression for the first 2000 s. Moreover, up to 1000 s, even the 5 MPa curve shows in a wide range a higher total strain than the 6 MPa curve.

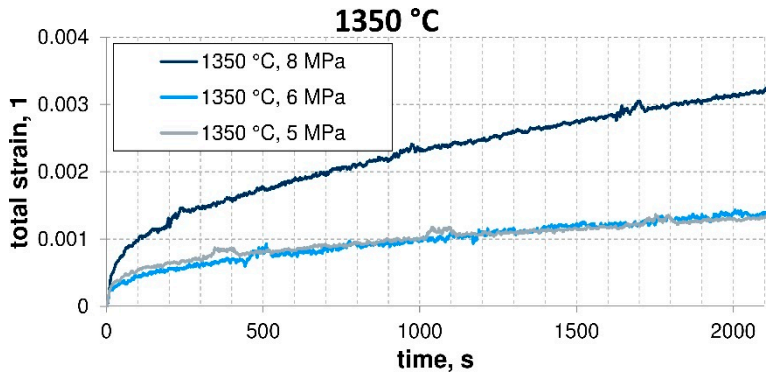

Figure 13. Total strain–time curves of the fired magnesia brick from experiments at 1350 °C and 5, 6 and 8 MPa compressive loads.

Experiments with the material used have shown that a load of 8 MPa does not cause significant creep deformations at temperatures below 1200 °C. Therefore, creep is not considered in the material model up to 1200 °C. The creep parameters were interpolated linear in the temperature range of 1200 °C up to 1350 °C. Based on the calculated creep data, a thermo-mechanical finite element analysis involving a heat-up process was conducted, for which the modelling details are shown in Figures 8 and 9. As in the linear elastic approach in the creep-based model, the thermal strain is the driving force for deformation and thermal stresses shown in Figure 14.

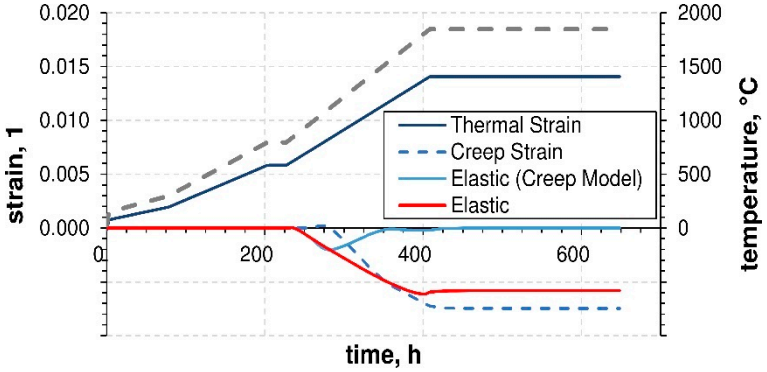

Figure 14. Temperature curve of the hot face, thermal strain, creep strain and elastic strain based on simulation results on center of the hot face.

In both models, the same heat-up curve was used resulting in equivalent thermal strains. Due to restrictions of the brick's thermal expansion, the mechanical strain (particularly elastic and inelastic strain) was built up.

The total strain curves of the steel shell in the circumferential direction shown in Figure 15 have the same progression up to approximately 1250 °C. Hence, creep strain reduced the total strain in the brick, resulting in a reduced expansion of the steel shell.

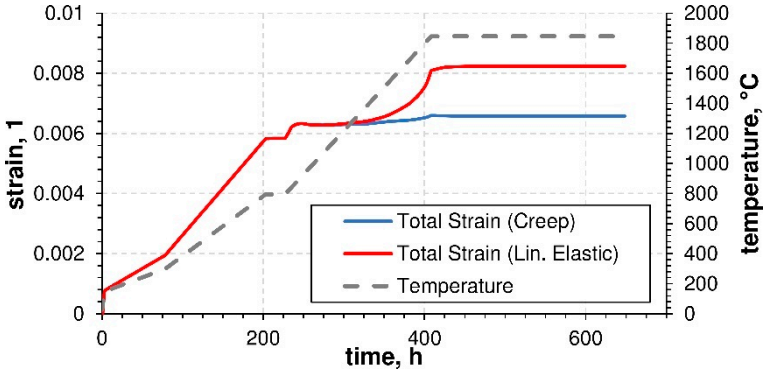

Figure 15. Comparison of the circumferential strain–time curve of the steel shell based on the linear elastic material model versus the Norton-Bailey approach together with the hot face temperature curve.

This mechanism led to a significant reduction in the von Mises stresses in the steel shell (Figure 16). The surface temperature of the steel shell in the model was kept constant at 50 °C due to water cooling. In contrast to the linear elastic finite element model, the considered creep constitutive model could predict a decrease in the occurring stresses by a factor of approximately three.

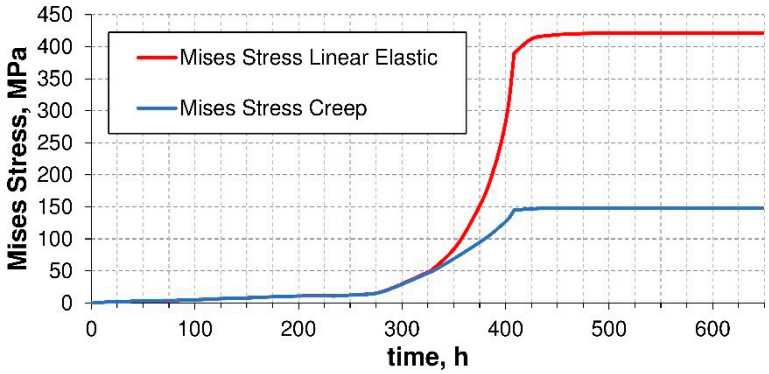

Figure 16. Von Mises stresses in the steel shell based on a simulation using the linear elastic approach in the center of the cold face.

4. Discussion

In the initial 2000 s, the curves generated for 5 and 6 MPa at 1350 °C have a similar progression (Figure 13). Even the 5 MPa curve showed a total strain higher than that of the 6 MPa curve. This can be explained by material inhomogeneities and the creep behavior of the material at the relative low temperature in combination with the precision of the testing device. Hence, this caused uncertainties for the inverse estimation procedure of the creep parameters, resulting in aberrations between the simulated and experimental curves as shown in Figure 10.

The measured total strain curves for 1425 °C and 1500 °C (depicted in Figures 11 and 12) show a satisfying agreement over the whole load range with the simulated curves. It is worth mentioning that Young's modulus and Poisson's ratio were determined in advance to simplify the complex inverse parameter estimation.

The creep of the investigated material was still in the primary stage as the values of a were negative (Table 5) for all tested temperatures and loads.

In this study, the thermal expansion due to the heat-up process and the constrain of the refractory material by the external steel shell were considered. The dominating stresses caused by the partially suppressed thermal expansion were compressive stresses in the refractory material and, therefore, a creep model based on uniaxial compressive load was used, although multiaxial compressive loads could occur in the refractory lining. So far, scientific research regarding material models for multiaxial

compressive creep of refractories seems to be lacking. Refractories show a porosity up to 20 vol%; therefore, it is still not known if the creep of refractories follows the classical creep behavior assuming constant volume. The models used here were based on the assumption of constant volume. The finite element analysis used to predict the steel shell's response to the thermal strains showed a realistic reduction in the von Mises stresses from approximately 420 MPa in the linear elastic case to 150 MPa using a creep model, as shown in Figure 16.

5. Conclusions

The primary creep stage behavior of a fired magnesia brick at high temperatures under uniaxial compressive conditions was investigated. Compressive creep tests under service-related loads and temperatures were conducted. The obtained creep deformations of the experimental investigations were subjected to an inverse analysis using the Levenberg-Marquardt optimization algorithm in MATLAB [15]. This iterative inverse method was used to determine the three parameters a, n and K for the Norton-Bailey creep law. Therefore, three curves at the same temperature but with different loads were used. The temperature range from 1150 °C up to 1500 °C was under research. The material started to show creep strain at 1200 °C under a load of 8 MPa. The uniaxial test was reproduced numerically using finite element analysis (FEA) and considering the Norton-Bailey creep model. The experimental and simulated total strain curves for a specific temperature were compared and showed good agreement. A three-dimensional part of a refractory structure was the subject of a further thermo-mechanically finite element analysis during the heat-up process. The objective was to compare the von Mises stresses in the steel shell by using a linear elastic material model for the lining compared with a Norton-Bailey creep model. Under the assumption that compressive stresses are predominant during heat-up, tensile creep behavior was not considered. Moreover, volume constancy was assumed in the creep model. The results of the FEA showed a significant reduction in the von Mises stresses in the steel shell from about 430 MPa to 150 MPa, which is much more realistic referring to the strength of the steel shell. The study has shown that the application of material creep models implemented in finite element analysis improves the prediction of stresses and strains in the refractory lining. Especially it shows more realistic stress values in the steel shell compared to commonly industrially used linear elastic material models.

Author Contributions: Conceptualization, G.U., D.R.K. and C.W.; Methodology, H.U.M., G.U. and B.L.; Validation, H.U.M., B.L. and D.R.K.; Formal Analysis, G.U. and B.L.; Investigation, B.L.; Resources, B.L.; Data Curation, B.L. and R.M.; Writing—Original Draft Preparation, G.U.; Writing—Review and Editing, H.U.M., B.L. and D.R.K.; Visualization, G.U.; Supervision, G.H.; Project Administration, G.U. and D.R.K. All authors have read and agreed to the published version of the manuscript.

Funding: This research received no external funding.

Acknowledgments: The authors gratefully thank the Chair of Ceramics (Montanuniversität, Leoben, Austria) for providing the efficient methodology to identify the creep law parameters and the scientific discussions.

Conflicts of Interest: This research was done in the Research and Development Center Leoben of RHI Magnesita, Austria. All the researchers are employees of RHI Magnesita.

References

1. Afshar, S.; Allaire, C. The corrosion of refractories by molten aluminum. *JOM* **1996**, *48*, 23–27. [CrossRef]
2. Allahevrdi, M.; Afshar, S.; Allaire, C. Additives and the corrosion resistance of aluminoslicate refractories in molten Al-5Mg. *JOM* **1998**, *50*, 30–34. [CrossRef]
3. Richerson, D.W. *Modern Ceramic Engineering: Properties, Processing and Use in Design*, 2nd ed.; Marcel Dekker, Inc.: New York, NY, USA, 1992; p. 834.
4. Munz, D.; Fett, T. *Ceramics Mechanical Properties, Failure Behavior, Material Selection*; Springer: Berlin/Heidelberg, Germany, 2001; pp. 227–229.
5. Blond, E.; Schmitt, N.; Hild, F.; Blumenfeld, P.; Poirier, J. Modelling of high temperature asymmetric creep behaviour of ceramics. *J. Eur. Ceram. Soc.* **2005**, *25*, 1819–1827. [CrossRef]

6. Wereszczak, A.A.; Ferber, M.K.; Kirkland, T.P.; Barnes, A.S.; Frome, E.L.; Menon, M.N. Asymmetric tensile and compressive creep deformation of hot-isostatically-pressed Y2O3-doped-Si3N4. *Eur. Ceram. Soc.* **1999**, *19*, 227–237. [CrossRef]
7. Kottada, R.S.; Chokshi, A.H. The high temperature tensile and compressive deformation characteristics of magnesia doped alumina. *Acta Mater.* **2000**, *48*, 3905–3915. [CrossRef]
8. Berest, P. *Viscoplasticity in Rock Mechanics in Geomaterials Constitutive Equations and Modelling*; Darve, F., Ed.; Elsevier Science Publishing Co.: Amsterdam, The Netherland, 1990; pp. 239–262.
9. Dusserre, G.; Nazaret, F.; Robert, L.; Cutard, T. Application of image correlation techniques to characterize asymmetric refractory creep during bending tests. *J. Eur. Ceram. Soc.* **2013**, *33*, 221–231. [CrossRef]
10. Mammar, A.S.; Gruber, D.; Harmuth, H.; Jin, S. Tensile creep measurements of ordinary ceramic refractories at service-related loads including setup, creep law, testing and evaluation procedures. *Ceram. Int.* **2016**, *42*, 6791–6799. [CrossRef]
11. Jin, S.; Harmuth, H.; Gruber, D. Compressive creep testing of refractories at elevated loads—Device, material law and evaluation technique. *J. Eur. Ceram. Soc.* **2014**, *34*, 4037–4042. [CrossRef]
12. Hosseini, E.; Holdsworth, S.; Mazza, E. Creep constitutive model considerations for high-temperature finite element numerical simulations. *JSA* **2012**, *47*, 341–349. [CrossRef]
13. Schachner, S.; Jin, S.; Gruber, D.; Harmuth, H. Three stage creep behavior of MgO containing ordinary refractories in tension and compression. *Ceram. Int.* **2019**, *45*, 9483–9490. [CrossRef]
14. Dusserre, G.; Valentin, O.; Nazaret, F.; Cutard, T. Experimental and numerical investigation of the asymmetric primary creep of a fibre reinforced refractory concrete at 1200 °C. *J. Eur. Ceram. Soc.* **2016**, *36*, 2627–2639. [CrossRef]
15. Marquardt, D.W. An algorithm for least-squares estimation of nonlinear parameters. *J. Soc. Ind. Appl. Math.* **1963**, *11*, 431–441. [CrossRef]